Geophysical Research Letters

RESEARCH LETTER
10.1029/2025GL118809

Ion-Scale Wave Emission and Absorption for Non-Maxwellian Velocity Distributions in the Inner Heliosphere

K. G. Klein[1], **D. Larson**[2], **R. Livi**[2], **M. M. Martinović**[1], **A. Rahmati**[2], **N. Shankarappa**[1], **M. Stevens**[3], **D. Verscharen**[4], **and P. Whittlesey**[2]

[1]Lunar and Planetary Laboratory, University of Arizona, Tucson, AZ, USA, [2]Space Science Laboratory, University of California, Berkeley, CA, USA, [3]Smithsonian Astrophysical Observatory, Cambridge, MA, USA, [4]Mullard Space Science Laboratory, University College London, Dorking, UK

Key Points:

- Non-Maxwellian velocity distributions observed by Parker Solar Probe/SPANi alter ion-scale wave behavior from bi-Maxwellian predictions
- Wave damping and growth rates are enhanced or decreased for selected time intervals, with variations up to a factor of three
- Differences between plasma responses derived from the observed and analytic distributions are robust against instrumental uncertainties

Supporting Information:

Supporting Information may be found in the online version of this article.

Correspondence to:

K. G. Klein,
kgklein@arizona.edu

Citation:

Klein, K. G., Larson, D., Livi, R., Martinović, M. M., Rahmati, A., Shankarappa, N., et al. (2026). Ion-scale wave emission and absorption for non-maxwellian velocity distributions in the inner heliosphere. *Geophysical Research Letters*, *53*, e2025GL118809. https://doi.org/10.1029/2025GL118809

Received 13 AUG 2025
Accepted 1 JAN 2026

Author Contributions:

Conceptualization: K. G. Klein, M. Stevens, D. Verscharen
Data curation: D. Larson, R. Livi, A. Rahmati, P. Whittlesey
Formal analysis: K. G. Klein, N. Shankarappa
Investigation: R. Livi, M. M. Martinović, N. Shankarappa
Methodology: K. G. Klein, M. Stevens, D. Verscharen
Project administration: M. Stevens
Software: K. G. Klein, D. Verscharen
Validation: D. Larson, R. Livi, A. Rahmati
Visualization: K. G. Klein, M. M. Martinović

Abstract

Hot and tenuous plasmas have velocity distribution functions (VDFs) significantly different from Maxwellian distributions. Characterizing how these differences impact wave damping and emission necessitates sophisticated methods for determining the associated dielectric plasma response. The Arbitrary Linear Plasma Solver (`ALPS`) is a tool for calculating such responses through numerical integration of arbitrary gyrotropic VDFs, rather than using analytical models, for example bi-Maxwellians, for the VDF. We consider dispersion relations for beam-driven instabilities, proton-cyclotron waves, and kinetic Alfven waves, derived using example VDFs from Parker Solar Probe/SPANi measurements during Encounters 22 and 23. The same kinds of waves are supported, but non-Maxwellian structures drive significant changes in the amount of energy absorbed by the charged particles or released into the waves, altering expected heating rates from these waves in the inner heliosphere.

Plain Language Summary

Hot, ionized gases, also known as plasmas, often do not experience enough collisions for them to be in thermal equilibrium. The non-equilibrium structures in the distribution of particle velocities in such systems change the collective behavior of waves. We consider examples of these changes using measurements from one of the plasma instruments on Parker Solar Probe, which measures the solar wind as close as 7 million kilometers from the Sun's surface, where non-equilibrium velocity structures are frequently observed. Sometimes these structures allow waves to propagate further before damping or change how energy from the damping is distributed between charged particle populations. In other examples, the non-equilibrium structures enhance the emission of waves. Our findings highlight the importance of sophisticated analyses of heating and instabilities in hot plasma systems in our solar system and throughout the universe.

1. Introduction

Plasma waves are a collective response of collections of charged particles. They transport mass, momentum, and energy, making them important for plasma system dynamics. Ion- and electron-scale waves are ubiquitously observed in many parts of the heliosphere, including the near-Sun environment (Bowen et al., 2020; Colomban et al., 2025; Liu et al., 2023; McManus et al., 2024), where they are hypothesized to contribute to the heating, acceleration, and evolution of the charged particle velocity distributions (VDFs) (Berčič et al., 2021; Colomban et al., 2024; Shankarappa et al., 2024).

Non-Maxwellian VDFs, frequently seen in weakly collisional plasmas such as the solar wind (Marsch, 2006; Verscharen et al., 2019), change the collective response of plasma systems. Most plasma wave studies assume a particular analytical model for the background plasma VDF, for example bi-Maxwellians [`WHAMP` (Roennmark, 1982), `NHDS` (Verscharen & Chandran, 2018), `PLUME` (Klein et al., 2025), and `BO` (Xie, 2019)] or κ-distributions [`DSHARK` (Astfalk et al., 2015)]. Motivated by observed departures from Maxwellianity at closer distances to the Sun (Verniero et al., 2022; T. A. Bowen et al., 2024) and predictions of deformed VDFs in marginally stable states (Isenberg, 2012), we characterize the impact of non-Maxwellian VDFs observed by Parker Solar Probe (Fox et al., 2015; Raouafi et al., 2023) on ion-scale waves.

To quantify the impact of non-Maxwellian VDFs on the plasma response, we use the numerical dispersion solver `ALPS` (Klein & Verscharen, 2025; Verscharen et al., 2018). Instead of assuming a particular analytical form for the background VDF, `ALPS` numerically integrates an arbitrary, gyrotropic input VDF, determining the complex dispersion relations and thus the solutions to the linear Vlasov–Maxwell theory it supports. There are notable

Writing – original draft: K. G. Klein
Writing – review & editing: M. M. Martinović, N. Shankarappa, D. Verscharen

changes in the damping and growth rates driven by VDF structures compared to best-fit, multi-component, bi-Maxwellian models. These changes alter how much energy waves deposit onto or remove from charged particles, necessitating the reëvaluation of heating models based upon bi-Maxwellian assumptions. Such changes have been seen when `ALPS` has been applied to numerical simulations (Fitzmaurice et al., 2025; Zhang et al., 2025) and in situ observations from Wind and MMS (Jiang et al., 2022, 2024; Walters et al., 2023). `ALPS` has not been applied to diagnose the impacts of non-Maxwellian structure on the generation and absorption of the cornucopia of waves seen in the inner heliosphere, and the resulting impact on solar wind heating and acceleration.

Section 2 describes our processing of SPANi data to produce gyrotropic VDFs on regular grids appropriate for numerical integration, with technical details found in the Supporting Information S1 appendix. Section 3 provides an overview of dispersion relations calculated from `ALPS`. Section 4 derives dispersion relations for both observed and bi-Maxwellian models for three case studies of different ion-scale waves germane to the inner heliosphere. Section 5 quantifies the impact of instrumental uncertainty on the derived dispersion relations, with concluding remarks in Section 6.

2. Producing Uniform, Gyrotropic VDFs From SPANi Observations

To determine the linear plasma response, we first convert measurements from SPANi (Livi et al., 2022), part of the SWEAP thermal plasma suite (Kasper et al., 2016) onboard Parker Solar Probe (PSP), into a data structure digestible by `ALPS`. We use L2 data, focusing on three accumulation intervals that are representative of typical conditions seen in the near-Sun solar wind; selected to highlight changes in beam-driven instabilities (2024-12-24:14:08:23), proton-cyclotron wave (PCW) absorption (2025-03-21:13:48:59), and kinetic Alfvén wave (KAW) damping (2025-03-22:02:19:00). Details on the characteristics of these intervals can be found in Section S1 of Supporting Information S1.

`ALPS` reads in a uniform, Cartesian grid of phase space densities as a function of $v_\perp/v_A$ and $v_\parallel/v_A$, where the velocity coördinates are normalized to the proton Alfvén velocity $v_A = B/\sqrt{4\pi n_p m_p}$, n_p and m_p are the proton density and mass, and $\boldsymbol{B}$ is the background magnetic field measured by the FIELDS magnetometer (Bale et al., 2016). The components $v_\perp$ and $v_\parallel$ of the particle velocity are taken in the directions perpendicular and parallel to $\boldsymbol{B}$. Details of the processing of the `ALPS` input grids from the SPANi measurements are discussed in Section S2 in Supporting Information S1.

If f_p is not resolved out to several thermal velocities, the derived plasma response is susceptible to discontinuities as resonant velocities pass over the edge of the measured VDF. To ensure coverage, we extrapolate the VDF out to sufficiently large velocities by adding a *collar* to the VDF. We fit $\log_{10}\left[f_p\left(v_\perp, v_\parallel\right)\right]$ to both single and two-component bi-Maxwellian models, producing the fitted distribution f_p^{fit}. Using the component model with the lower residual error, see Table S2 in Supporting Information S1, we evaluate f_p^{fit} along 10 uniformly spaced rings in $\left(v_\perp, v_\parallel\right)$ with radii ranging from the largest measured velocity $v^{\max}/v_A$ to $v^{\max}/v_A + 1$, illustrated in Figure S2c Supporting Information S1.

Combining the collar and observed VDF, we perform a thin-plate spline interpolation (Donato & Belongie, 2002; Powell, 1994; Verscharen et al., 2018; Wood, 2003), creating a regular grid in $\left(v_\perp, v_\parallel\right)/v_A$, green contours in the top rows of Figures 2–4, producing the *observed* model. We evaluate the best fit *bi-Maxwellian* model using f_p^{fit}, which can have one or two components, on the same regular grid, shown as purple contours. We treat the electrons as an isotropic Maxwellian background VDF with the same temperature as the protons and appropriate density and drift speed to enforce quasineutrality and zero net current using an analytic bi-Maxwellian susceptibility tensor; see Klein and Verscharen (2025); Appendix B.

3. Calculating Dispersion Relations for Arbitrary Gyrotropic VDFs

The Arbitrary Linear Plasma Solver (`ALPS`) solves the linear Vlasov–Maxwell dispersion relation for a hot, magnetized plasma (Klein & Verscharen, 2025; Verscharen et al., 2018), allowing for any number of particle species with arbitrary gyrotropic background VDFs supporting normal modes with any direction of propagation with respect to the background magnetic field $\boldsymbol{B}$. `ALPS` numerically integrates over the appropriate functions of velocity gradients of the background VDFs that comprise the plasma wave equation rather than assuming a bi-

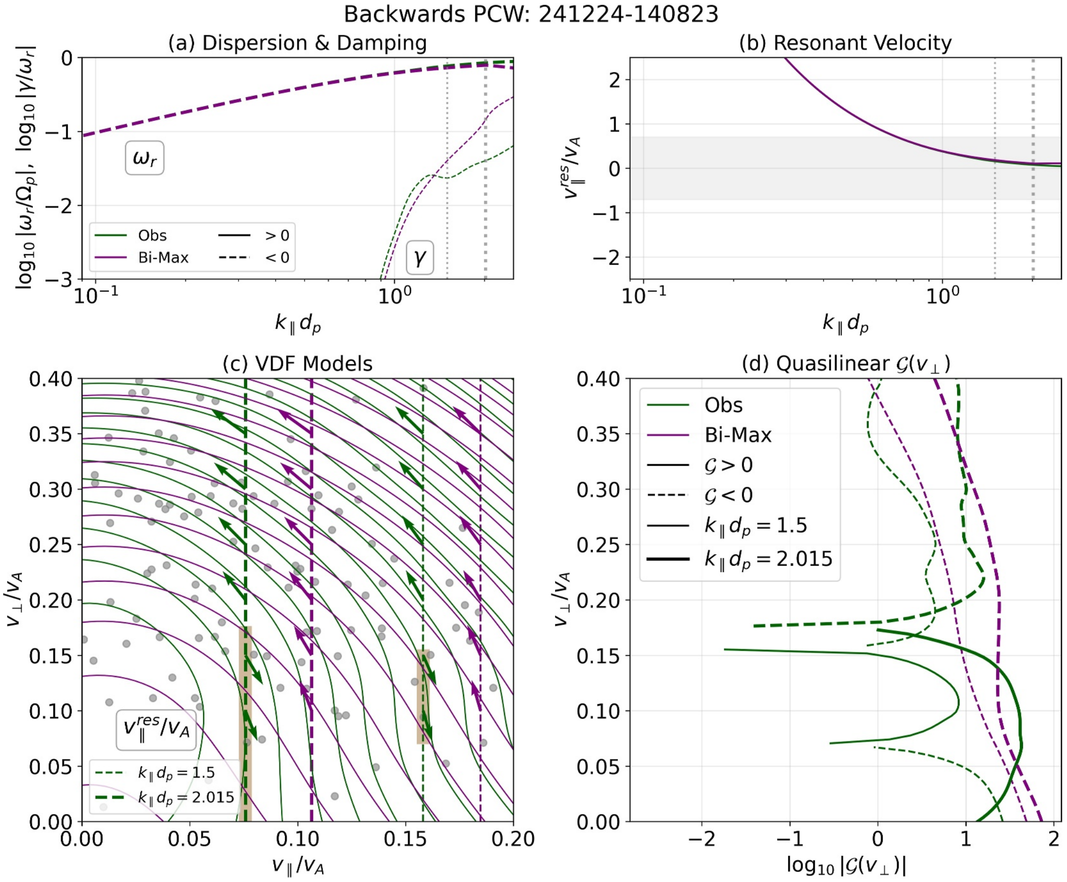

Figure 1. Calculation of wavevector-dependent quasilinear emission or absorption $\mathcal{G}\{f_p[v_\parallel^{\rm res}(k_\parallel), v_\perp]\}$ for the backward parallel propagating PCW for 2024-12-24 14:08:23, highlighting resonant behavior at $k_\parallel d_p = 1.5$ and 2.015 (thin and thick dashed lines) for the bi-Maxwellian and Observed models (purple and green). (a) Real frequency ω_r and damping rates γ. (b) Resonant velocity $v_\parallel^{\rm res}$. (c) Contours of VDF models overlaid with $v_\parallel^{\rm res}$ for the selected $k_\parallel d_p$. Dashed lines indicate resonant velocities associated with selected wavevectors. Arrows indicate tangents to circles centered at $\omega_r/k_\parallel$ and brown highlights $v_\perp$ ranges where particles lose energy, which is gained by the electromagnetic wave. (d) $\mathcal{G}(v_\perp/v_A)$ evaluated at the two selected $k_\parallel d_p$ values for both models, with $\mathcal{G} > 0$ ($\mathcal{G} < 0$) signifying wave emission (absorption).

Maxwellian shape; the full set of equations solved are listed by Verscharen et al. (2018). After calculating complex dispersion relations in the form $\omega(\mathbf{k}) = \omega_r(\mathbf{k}) + i\gamma(\mathbf{k})$, where ω is the complex wave frequency, $\boldsymbol{k}$ is the wavevector, and ω_r and γ are the real and imaginary parts of ω, `ALPS` determines the associated eigenfunctions of density and velocity fluctuations and electromagnetic fields. `ALPS` further calculates the damping rate onto each component j, $\gamma_j/|\omega_r|$, following Quataert (1998) and Klein et al. (2020).

To identify what parts of $f_p(v_\perp, v_\parallel)$ contribute to a wave's behavior, we apply quasilinear theory (Kennel & Petschek, 1966; Verscharen & Chandran, 2013). The resonant coupling between wave and VDF can be modeled by applying the operator

$$\mathcal{G} \equiv \left(1 - \frac{k_\parallel v_\parallel}{\omega_r}\right)\frac{\partial}{\partial v_\perp} + \frac{k_\parallel v_\perp}{\omega_r}\frac{\partial}{\partial v_\parallel} \tag{1}$$

to $f_p(v_\perp, v_\parallel)$. We highlight the regions of the VDF driving wave growth and damping as a function of scale by constructing functions that depend on the wavevector components $k_\parallel$ or $k_\perp$, applying $\mathcal{G}$ to f_p across $v_\perp$ at the resonant parallel velocity associated with each wavevector,

$$\frac{v_{\parallel}^{\mathrm{res}}(\mathbf{k})}{v_A} = \frac{\omega_{\mathrm{r}}(\mathbf{k})/\Omega_p - n}{k_{\parallel} d_p}, \tag{2}$$

where d_p is the proton inertial length. The resonant integer n determines the order of the relevant resonance, which is related to the polarization of the wave. For waves with purely left-handed (right-handed) circular polarization, only the resonance with $n = +1$ ($n = -1$) is accessible. The Landau resonance acts through $n = 0$.

As an example, for a backwards parallel propagating proton cyclotron wave associated with interval 2024-12-24 14:08:23, we determine $\omega_{\mathrm{r}}(k_{\parallel})$ and $\gamma(k_{\parallel})$ for both the bi-Maxwellian and Observed models and the associated resonant velocity, Equation 2, shown in Figures 1a and 1b. To highlight the parts of $f_p(v_{\perp}, v_{\parallel})$ that transfer energy to or draw energy from the wave, we select two wavevectors, $k_{\parallel} d_p = 1.5$ and 2.015. The resonant velocity for these wavevectors are shown as vertical lines on top of contours of constant $f_p(v_{\perp}, v_{\parallel})$ for the two models in Figure 1c. For a given $v_{\parallel}^{\mathrm{res}}$, particles are scattered tangent to semi-circles in velocity space with origins centered at the parallel phase velocity of the wave, $(v_{\perp}, v_{\parallel}) = (0, \omega_{\mathrm{r}}/k_{\parallel})$. If the particles are scattered to higher kinetic energy, the wave loses energy. If the particles are scattered to lower kinetic energy, shown with brown highlighting in Figure 1c, the wave gains energy.

The amount of energy gained or lost is proportional to $\mathcal{G}\left\{f_p\left[v_{\parallel}^{\mathrm{res}}(k_{\parallel}), v_{\perp}\right]\right\}$, shown for the selected wavevectors for both models in Figure 1d. In the bi-Maxwellian model, the wave absorbs energy at all $v_{\perp}$, while there is emission for select ranges of $v_{\perp}$ from the Observed model. The overall damping or growth of the wave is determined by integrating over $v_{\perp}$; by comparing models as a function of velocity, we determine which parts of the distribution are changing the linear response of the plasma. In Figures 2–4, panels f and g, we expand this calculation to a range of wavevectors.

4. Impacts on Plasma Wave Response

We consider three ion-scale wave types for three SPANi intervals, specifically kinetic Alfvén waves (KAWs, Section 4.1), proton-cyclotron waves (PCWs, Section 4.2), and fast mode/whistlers (FMWs, Section 4.3). We describe forward and backward propagating waves as those moving along or against the local magnetic field direction.

4.1. Reduction of Kinetic Alfvén Wave Damping

KAWs are the extension of the Alfvén dispersion surface with $k_{\perp}\rho_p \gtrsim 1$ and $k_{\parallel} d_p \ll 1$, where ρ_p is the thermal proton gyroradius. Since this mode mediates the Alfvénic turbulent cascade at ion scales (Drake et al., 2013; Howes & Nielson, 2013; Schekochihin et al., 2009), KAW damping rates are used to estimate the deposition of energy onto the protons and the overall partition of energy between protons and electrons in a variety of astrophysical contexts (Gorman & Klein, 2024; Howes, 2010; Quataert, 1998; Shankarappa et al., 2023; TenBarge & Howes, 2013).

To discern impacts of VDF structure on KAW damping, we consider interval 2025-03-21 13:48:59, processed into `ALPS` format in the top row of Figure 2, with bulk parameters listed in Table S1 of Supporting Information S1. The VDF has a clear secondary population extending beyond $v_{\parallel} \sim -2v_A$, with broadening similar to observed "hammerhead" structures (Verniero et al., 2020, 2022). We follow the Alfvénic solution holding $k_{\parallel} d_p = 10^{-3}$ constant and varying $k_{\perp} d_p \in [10^{-2}, 4]$.

The KAW solutions have qualitatively identical ω_{r} for the two models, visually overlapping for the backwards solution in Figure 2, while the damping rates γ differ. Resonant wavevectors where the bi-Maxwellian and Observed models' dispersion relations show significant differences are bounded by brown lines in Figure 2. For the backwards KAW, the observed model's total damping rate is reduced to $\approx 80\%$ of the bi-Maxwellian model at $k_{\perp}\rho_p \ll 1$. At proton kinetic scales, $k_{\perp} d_p \gtrsim 1$, the proton damping γ_p increases by a factor of three compared to the bi-Maxwellian model. For the forwards KAW, γ_p at MHD scales is slightly larger for the observed model than then bi-Maxwellian model. At $k_{\perp} d_p \sim 1$, the protons in the observed model release rather than absorb energy, leading to a reduction of the total damping rate for the observed model by 50% compared to the bi-Maxwellian

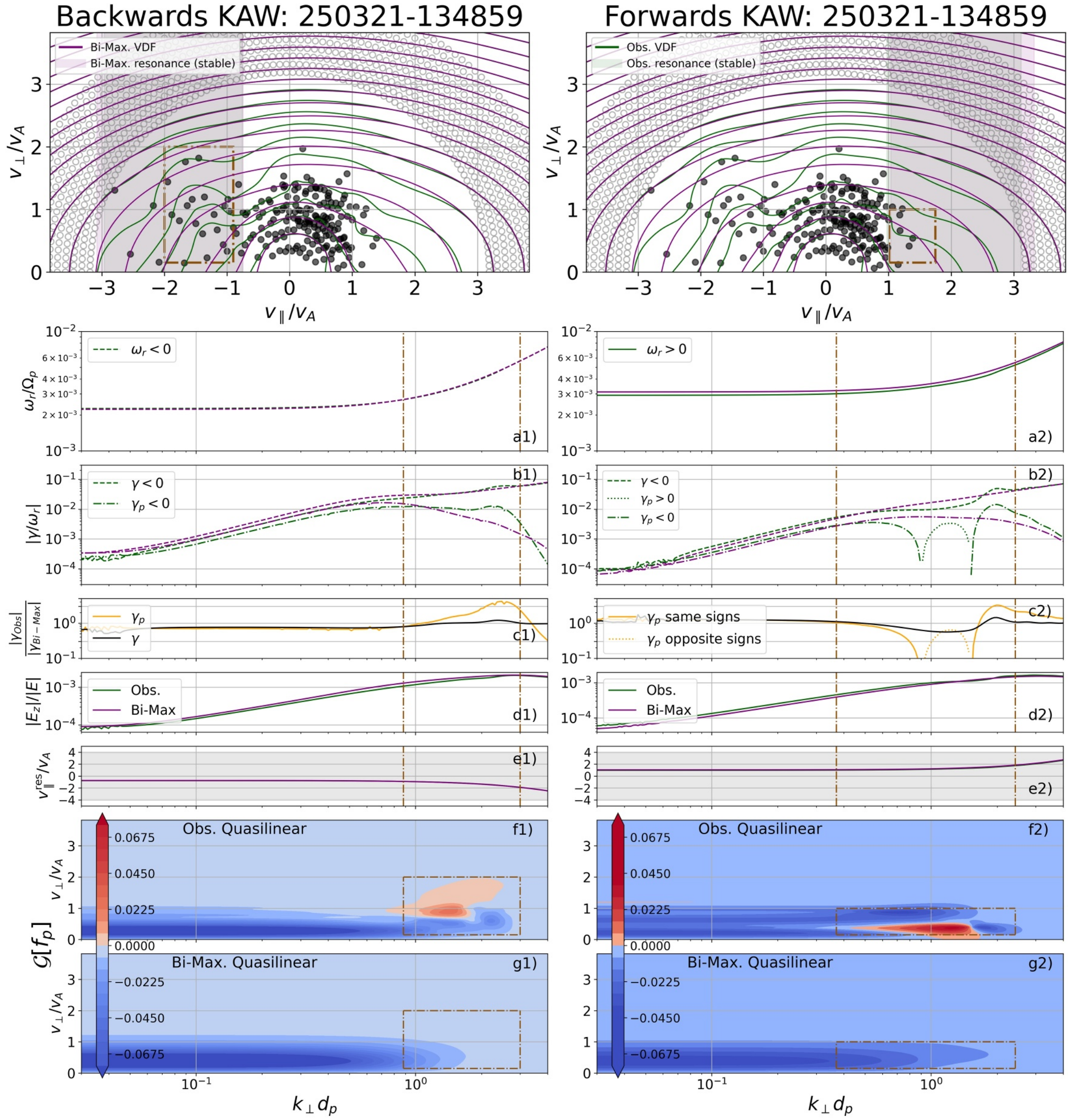

Figure 2. Backward (left) and forward (right) KAW dispersion relations as a function of $k_\perp d_p$ for interval 2025-03-21 13:48:59. (Top) Contours of observed (green lines) and bi-Maxwellian (purple) VDF models, and underlying observed points (solid dots) and constructed collar (open). Regions of $n = 0$ resonance, Equation 2, are indicated by shading. (a) Real frequency ω_r/Ω_p, (b) total damping/growth rate $\gamma/|\omega_r|$ and proton contribution to the damping/growth rate $\gamma_p/|\omega_r|$, (c) damping rate ratio $\gamma_p^{\mathrm{Obs}}/\gamma_p^{\mathrm{bi\text{-}Max}}$, (d) relative amplitude of the parallel electric field $|E_z|/|E|$. (e) Resonant velocity for the Landau resonance, Equation 2; grey shading indicates the region of resolved $v_\parallel/v_A$ for the VDF models. (f, g) Quasilinear operator $\mathcal{G}\left\{f_p\left[v_\parallel^{\mathrm{res}}(k_\perp), v_\perp\right]\right\}$ applied to the two models indicating wave absorption (blue) or emission (red). The brown dashed lines bound velocity-wavevector regions associated with significant differences between the models' dispersion relations.

model. As the predicted electron damping is a higher amplitude, the KAW does not become unstable; the total Observed damping rate is reduced to 50% of the bi-Maxwellian model.

To discern the difference between the bi-Maxwellian and observed models, we first note the small difference in the amplitude of the fluctuating parallel electric field driving the Landau damping, $|E_z|/|E|$, which is slightly larger in the bi-Maxwellian model for the backwards KAW and in the observed model for the forwards KAW. The resonant velocities $v_\parallel^{\mathrm{res}}(k_\perp)$ for $n = 0$ are nearly identical for the two models, given they have nearly identical $\omega_r(k_\perp)$.

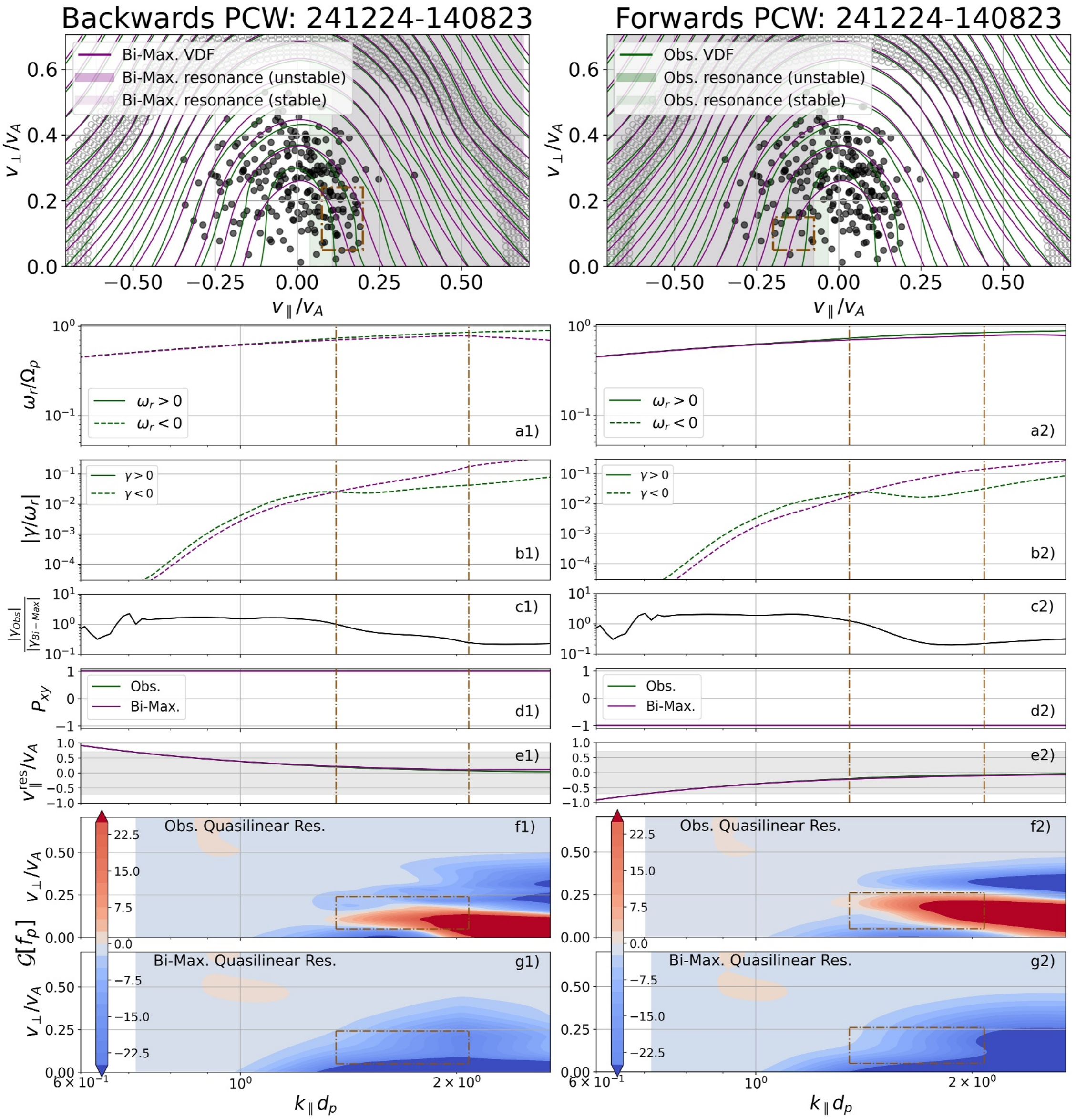

Figure 3. Backward (left) and forward (right) PCW dispersion relations for interval 2024-12-24 14:08:23. Organized as Figure 2, but as a function of varying $k_\parallel d_p$ with constant $k_\perp d_p = 10^{-3}$, and regions of $n = \pm 1$ resonance, Equation 2, are indicated by shading. The fifth row replaces $|E_z|/|E|$ with polarization $\mathcal{P}$, Equation 3.

More significant differences can be seen in the evaluation of $\mathcal{G}\left\{f_p\left[v_\parallel^{\mathrm{res}}(k_\parallel), v_\perp\right]\right\}$, which characterizes which part of the VDF releases or absorbs energy. These regions of $(k_\perp d_p, v_\perp/v_A)$ and $(v_\parallel, v_\perp)/v_A$ that correspond to the ranges of $k_\perp d_p$ with significant differences between the solutions are enclosed in brown bounding boxes in Figure 2. At $k_\perp d_p \ll 1$, both models have similar $\mathcal{G}[f_p]$ structure, entirely absorbing wave energy and mostly confined to $v_\perp \lesssim v_A$. Approaching $k_\perp d_p \gtrsim 1$, the emission and absorption structure changes for the observed model.

For the backwards KAW, particles from the observed model with $v_\perp < v_A$ continue to absorb, contrasting with a lack of absorbing structure for the bi-Maxwellian case, while for a limited range of wavevectors, particles with $v_\perp \gtrsim v_A$ release some energy. The net effect is an increase of the proton contribution to the damping rate between $k_\perp d_p \in [1,3]$, peaking at $\gamma_p^{\mathrm{Obs}} = 3\gamma_p^{\mathrm{bi\text{-}Max}}$ at $k_\perp d_p \approx 2.5$. This different response is due to differences in the VDF structure at $v_\parallel/v_A \sim -1$ and $v_\perp \in [0,2]v_A$, where a dense secondary proton population increases the proton damping rate for the observed model at $k_\perp d_p \sim 1$.

For the forwards KAW, the particles releasing energy for the observed model are those at $v_\perp < v_A$, whose contribution leads to an overall emission of energy from the protons for the observed model. The observed VDF structure responsible is a sharp velocity gradient at $(v_\parallel, v_\perp)/v_A \sim (1.25, 0.5)$, indicated with the brown dashed lines in the top row of Figure 2.

The structures driving significant changes from the bi-Maxwellian model arise at $v_\parallel \approx v_A$, which serves as an indirect sign of quasilinear flattening of the VDF due to Landau damping near $v_\parallel^{\mathrm{res}}$ for $n = 0$. Such signatures, previously seen further from the Sun, for example Marsch (2006), He et al. (2015), are generally expected to lead to a reduction of the proton damping rate, altering the partition of energy between the particle species, both in the inner heliosphere and in other systems of weakly collisional Alfvénic turbulence, impacting predictive models for Q_j as a function of plasma and bulk system parameters (Howes, 2024).

To assess the impact of modeled damping rates on Q_p/Q_e, we convolve the damping rates $\gamma_s^{\mathrm{model}}$ with the observed magnetic power spectra $b_{k,\mathrm{turb}}$ to determine the heating rate Q_s, see Section S3 in Supporting Information S1 and Shankarappa et al. (2024) more details. We find $Q_p^{\mathrm{obs}}\left(Q_p^{\mathrm{bi\text{-}Max}}\right) = -3.4(-4.2) \times 10^4$ J/s for the forward KAW, and $-7.6(-10.0) \times 10^4$ J/s for the backwards KAW. This represents a 24% and 19% reduction in the proton heating rates for the forward and backwards solutions.

4.2. Marginal Stability of Proton Cyclotron Waves

The near-Sun solar wind is filled with PCWs (Bowen et al., 2020; Liu et al., 2023), which contribute to plasma heating (T. A. Bowen et al., 2024; Shankarappa et al., 2024). This cyclotron heating, like Landau damping, modifies the VDF through quasilinear diffusion, leading to a marginally stable state that is effectively transparent to this mode (Isenberg, 2012; Isenberg & Vasquez, 2015). We consider interval 2024:12:24-14:08:23, investigating the forward and backward parallel propagating Alfvén/PCW solution in Figure 3 with bulk parameters in Table S1 of Supporting Information S1. We hold $k_\perp d_p = 10^{-3}$ constant, varying $k_\parallel d_p$.

We define the polarization of the perpendicular electric field as

$$\mathcal{P} = \frac{|E_R| - |E_L|}{|E_R| + |E_L|}, \tag{3}$$

where $E_{R,L} \equiv (E_x \mp iE_y)/\sqrt{2}$. Both the bi-Maxwellian and observed PCWs have the same polarizations, right-handed for the backward waves and left-handed for the forward waves.

As there is no prominent secondary population in this interval, the VDF exhibits almost mirror symmetry around $v_\parallel = 0$ and the forward and backward PCWs show similar behavior in terms of their dispersion relation and polarization properties. At $k_\parallel \rho_p \ll 1$, ω_{r} for the two models are nearly identical. For $k_\parallel d_p \gtrsim 1$, the values begin to diverge, with the bi-Maxwellian ω_{r} dipping to lower values due to the impact of stronger damping on the dispersion relation. Both the forward and backward PCWs have altered damping rates for the observed model, slightly increasing at $k_\parallel d_p \lesssim 1$ but with a significant reduction at $k_\parallel d_p > 1$, dropping by more than a factor of three.

The wavevectors with significant differences in $\gamma\left(k_\parallel\right)$ are bounded by brown dashed lines in Figure 3. Looking at energy emission and absorption via $\mathcal{G}\left\{f_p\left[v_\parallel^{\mathrm{res}}\left(k_\parallel\right), v_\perp\right]\right\}$, the bi-Maxwellian model almost entirely absorbs energy from the PCW, with the strongest absorption near $|v_\parallel| \sim 0.2v_A$ and $v_\perp \lesssim 0.125v_A$. For the observed model, particles in a band of $v_\perp$ counteract the absorption, releasing energy while particles with larger and smaller $v_\perp$ absorb energy. This does not produce an overall instability, but significantly reduces the total damping onto the protons. It is the sharp velocity gradient for these values of $v_\perp/v_A \sim 0.1$—effectively equivalent to larger $T_\perp/T_\parallel$ values over a narrow range of resonant velocities—that drives this narrow region of velocity space to release energy, overall moving the VDF towards a marginally stable state. As with the KAWs, this reduction in the proton damping rate inhibits the immediate dissipation of the wave. These more transparent VDFs enable PCWs to propagate further before damping away, transporting energy over larger distances than would be expected for bi-Maxwellian plasmas.

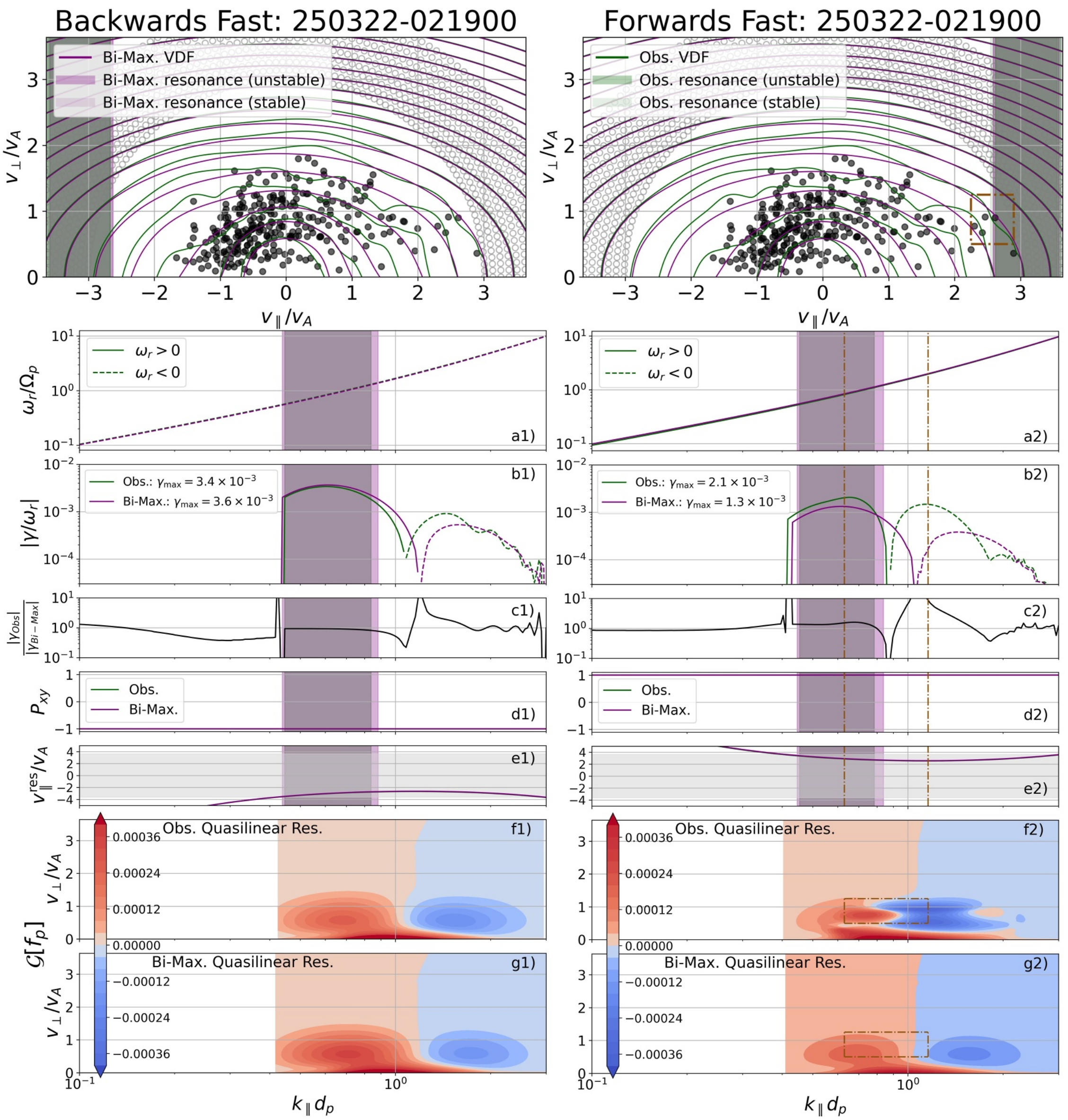

Figure 4. Backward (left) and forward (right) parallel FMW wave dispersion relations for interval 2025-03-22 02:19:00. Organized as Figure 3. Regions of $n = \pm 1$ resonance, Equation 2, are indicated by shading, with stable/unstable velocities having lighter/darker.

4.3. Enhancement of Beam-Driven Instabilities

Drifting secondary populations are capable of driving instabilities, for example Table 4 of Verscharen et al. (2019). An example drift-driven instability is right-handed fast-magnetosonic/whistler (FM/W) wave instability. Right-handed waves likely driven by such instabilities have been frequently observed in the inner heliosphere by PSP (He et al., 2022; Shi et al., 2025). We consider an interval susceptible to this instability, 2025-03-22 02:19:00, shown in Figure 4, where a pronounced proton beam is present; bulk parameters are given in Table S1 of Supporting Information S1. We fix $k_\perp d_p = 10^{-3}$, and vary $k_\| d_p$ up to 3.

As with the KAWs, ω_r for the FM/W waves is nearly identical for the two models. The growth rates for the backwards propagating waves are nearly the same, with $\gamma_{max}/|\omega_r| = 3.4 \times 10^{-3}$ for the observed model and $\gamma_{max}/|\omega_r| = 3.2 \times 10^{-3}$ for the bi-Maxwellian model. As the polarization $\mathcal{P}$ is left-handed, the solution couples with the back half of the VDF, up to $v_\| \sim -2.75 v_A$ at $k_\| d_p \sim 1$, where the dispersive nature of the solution bends $v_\|^{res}$ away from the center of the VDF. Given the velocities resolved by SPANi, the backwards FM/W wave

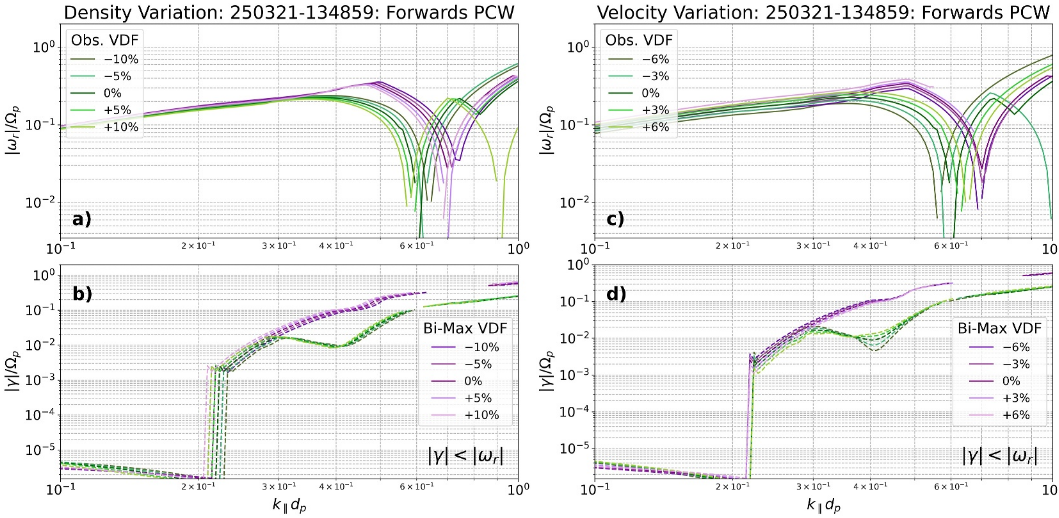

Figure 5. Real frequency $|\omega_r|/\Omega_p$ (a, c) and damping rate γ/Ω_p (b, d) for the forward PCW for bi-Maxwellian (purple) and observed models (green) for 2025-03-21 13:48:59. (left) Proton density varies by $\pm(5, 10)\%$. (right) Proton bulk velocity varies by $\pm(3, 6)\%$.

only resonates with the collar and the extrapolated region, not the region directly supported by observations. It is therefore unsurprising that the dispersion relations are similar for the observed and bi-Maxwellian models.

For the forward FM/W wave, the resonance couples with regions of the VDF directly supported by SPANi measurements. We see a slightly narrower region of unstable parallel wavevectors for the observed model, but an increase in the fastest growing mode from $\gamma/|\omega_r| = 1.3 \times 10^{-3}$ to 2.1×10^{-3}, a 61% increase in the growth rate. The wavevectors leading to significant differences in the dispersion relation between the two models are bounded with brown dashed lines. Evaluating $\mathcal{G}[f_p]$ reveals that the enhancement in the instability is driven by the steeper velocity gradient in the secondary population at $(v_\parallel, v_\perp) \sim (2.5, 1)v_A$.

5. Impact of Uncertainty in Bulk Parameter Determination

We next consider errors in proton density, which impact the v_A normalization, and in plasma velocity, which informs the spacecraft-to-plasma frame transformation, on the construction of the `ALPS` grids. Other sources of uncertainty associated with the processing of the SPANi data into a regular, gyrotropic velocity grid are treated in the Supporting Information S1, (see Section S2 in Supporting Information S1.) We focus on forward PCWs associated with interval 2025-03-21 13:48:59; similar results are found for other intervals and modes.

We first vary n_p by ±5% and ±10%, consistent with typical instrumental uncertainty from the quasi thermal noise spectroscopy (Moncuquet et al., 2020) used for SPANi calibration, leading to offsets in v_A of ±2.23% and ±3.16%. The resulting dispersion relations are shown in the left panels of Figure 5. For this interval, the resonant proton population in the beam is sufficiently dense to damp the PCWs strongly at $k_\parallel d_p \sim 0.6$, leading ω_r to change sign.

Variations in n_p change the wavevector where the solution departs from $\omega_r \approx k_\parallel v_A$ or the typical asymptotic maximum (cf. Howes et al., 2014; Eqn. 14), but the two model solutions remain clearly distinguishable. As seen for the PCWs from 2024-12-24 14:08:23, the observed damping rates are significantly reduced compared to the bi-Maxwellian model. For this interval, the reduction at some scales is by nearly an order of magnitude. Variations in γ due to variations in n_p are minimal, retaining a clear distinction between the dispersion relations from the two models.

We next vary U_{sw}, which is used to transform the SPANi measurement to the plasma frame prior to the `ALPS` array construction. We consider variations of ±3% and ±6%, consistent with expectations of uncertainty from SPANi, shown in the right panels of Figure 5. As with the density variations, we see qualitative changes to both ω_r and γ, with increased velocity slightly increasing ω_r. However, the significant difference in the damping rates between the two models remains, and the solutions for both models are distinguishable over most scales above the proton scales where the solution resonates with observationally resolved velocities.

6. Conclusions

For selected SPANi observations, significant differences in the linear damping behavior are observed for three different kinds of ion-scale waves. These changes are driven by structures in the VDF that are not captured by bi-Maxwellians models. Including a secondary bi-Maxwellian population is not sufficient to reproduce significant enhancements in growth rates or decreases in damping rate from our observed model. The altered plasma response lowers the predicted KAW and PCW heating rates and reduces the relative absorption of energy by the protons compared to the electrons. If such reductions are general features of Alfvénic turbulence, this finding impacts interpretations of ion and electron temperatures in a variety of astrophysical systems, for example Chael et al. (2018).

The reduction in PCW damping rates offers a potential explanation for the persistence of coherent ion-scale PCWs in the inner heliosphere, enabling them to propagate further from where they are generated. Other mechanisms, for example the *Helicity Barrier* (Meyrand et al., 2021; Squire et al., 2022), may also contribute to the presence of PCWs in the near-Sun environment. As shown by Zhang et al. (2025), heating in imbalanced turbulence asymmetrically deforms ion VDFs, altering the plasma response from bi-Maxwellian predictions. While including instrumental uncertainties in bulk plasma parameters quantitatively change the derived dispersion relations, the qualitative differences between the observed and bi-Maxwellian waves remain robust.

Such calculations are possible due to SPANi's energy and temporal resolution, and thus can be performed using other high resolution measurements, c f. Studies using MMS (Afshari et al., 2024) or Solar Orbiter (Zhu et al., 2023). Continued improvements in measuring VDFs, for example as discussed by Wilson et al. (2022) or implemented on future missions (Goodrich et al., 2023; Klein, Spence, et al., 2023; Nicolaou et al., 2020) will enable further exploration of the impact of VDF structure on plasma wave behavior in space plasmas. Future work will compare against more sophisticated representations of VDFs, for example Hermite–Laguerre expansions (Coburn et al., 2024; Wu et al., 2023), Slepian representations (Bharati Das & Terres, 2025), or Gaussian Process Regression (T. Bowen et al., 2024) that may more accurately capture the velocity gradients than the thin-plate spline interpolation implemented here.

Conflict of Interest

The authors declare no conflicts of interest relevant to this study.

Data Availability Statement

The `ALPS` code is available via an open source BSD 2-Clause License at https://github.com/danielver02/ALPS with a full tutorial on its use at https://danielver02.github.io/ALPS/ (Klein, Verscharen, et al., 2023).

The spacecraft data for this Letter are openly available from the NASA Space Physics Data Facility (Bale et al., 2020; Livi et al., 2020). Additional SWEAP data and information are available at the SWEAP web page http://sweap.cfa.harvard.edu/Data.html.

Acknowledgments
The SWEAP Investigation and this publication are supported by the PSP mission under NASA contract NNN06AA01C. This project received support from UCL's Advanced Research Computing Centre through the Open Source Software Sustainability Funding scheme. This study benefited from support by the International Space Science Institute (ISSI) in Bern, through ISSI International Team project 24-612 ("Excitation and dissipation of kinetic-scale fluctuations in space plasmas"). K.G.K was supported in part by NASA Grants 80NSSC19K0912, 80NSSC24K0171, and 80NSSC24K0724. D.V. is supported by STFC Consolidated Grant ST/W001004/1.

References

Afshari, A. S., Howes, G. G., Shuster, J. R., Klein, K. G., McGinnis, D., Martinović, M. M., et al. (2024). Direct observation of ion cyclotron damping of turbulence in Earth's Magnetosheath plasma. *Nature Communications*, *15*(1), 7870. https://doi.org/10.1038/s41467-024-52125-8

Astfalk, P., Görler, T., & Jenko, F. (2015). DSHARK: A dispersion relation solver for obliquely propagating waves in bi-kappa-distributed plasmas. *Journal of Geophysical Research (Space Physics)*, *120*(9), 7107–7120. https://doi.org/10.1002/2015JA021507

Bale, S. D., Goetz, K., Harvey, P. R., Turin, P., Bonnell, J. W., Dudok de Wit, T., et al. (2016). The FIELDS instrument suite for solar probe plus—Measuring the coronal plasma and magnetic field, plasma waves and turbulence, and radio signatures of solar transients. *Space Science Reviews*, *204*(1–4), 49–82. https://doi.org/10.1007/s11214-016-0244-5

Bale, S. D., MacDowall, R. J., Koval, A., Pulupa, M., Quinn, T., & Schroeder, P. (2020). Psp fields fluxgate magnetometer (mag) magnetic field vectors, radial-tangential-normal, RTN coordinates, full resolution, level 2 (l2), 3.413 Ms data 2020 data [Dataset]. *NASA Space Physics Data Facility*. https://doi.org/10.48322/0yy0-ba92

Berčič, L., Verscharen, D., Owen, C. J., Colomban, L., Kretzschmar, M., Chust, T., et al. (2021). Whistler instability driven by the sunward electron deficit in the solar wind. High-cadence Solar Orbiter observations. *Astronomy and Astrophysics*, *656*, A31. https://doi.org/10.1051/0004-6361/202140970

Bharati Das, S., & Terres, M. (2025). Recovering ion distribution functions. I. Slepian reconstruction of velocity distribution functions from MMS and solar Orbiter. *The Astrophysical Journal*, *982*(2), 96. https://doi.org/10.3847/1538-4357/adb6a0

Bowen, T., Azari, A., Klein, K. G., Ervin, T., & Isenberg, P. A. (2024). Employing probabilistic machine learning in understanding wave-particle interactions. *AGU Fall Meeting Abstracts*, *2024*, SH21E–287.

Bowen, T. A., Mallet, A., Huang, J., Klein, K. G., Malaspina, D. M., Stevens, M., et al. (2020). Ion-scale electromagnetic waves in the inner heliosphere. *The Astrophysical Journal Supplement Series*, *246*(2), 66. https://doi.org/10.3847/1538-4365/ab6c65

Bowen, T. A., Vasko, I. Y., Bale, S. D., Chandran, B. D. G., Chasapis, A., Dudok de Wit, T., et al. (2024). Extended cyclotron resonant heating of the turbulent solar wind. *The Astrophysical Journal Letters*, *972*(1), L8. https://doi.org/10.3847/2041-8213/ad6b2e

Chael, A., Rowan, M., Narayan, R., Johnson, M., & Sironi, L. (2018). The role of electron heating physics in images and variability of the Galactic Centre black hole Sagittarius A. *Monthly Notices of the Royal Astronomical Society*, *478*(4), 5209–5229. https://doi.org/10.1093/mnras/sty1261

Coburn, J. T., Verscharen, D., Owen, C. J., Maksimovic, M., Horbury, T. S., Chen, C. H. K., et al. (2024). The regulation of the solar wind electron heat flux by wave–particle interactions. *The Astrophysical Journal*, *964*(1), 100. https://doi.org/10.3847/1538-4357/ad1329

Colomban, L., Agapitov, O. V., Krasnoselskikh, V., Choi, K. E., Kretzschmar, M., Dudok de Wit, T., et al. (2025). Polarization properties of whistler waves from the first 17 parker solar probe encounters. *Geophysical Research Letters*, *52*(10), e2025GL114622. https://doi.org/10.1029/2025GL114622

Colomban, L., Kretzschmar, M., Krasnoselkikh, V., Agapitov, O. V., Froment, C., Maksimovic, M., et al. (2024). Quantifying the diffusion of suprathermal electrons by whistler waves between 0.2 and 1 AU with solar orbiter and parker solar probe. *Astronomy and Astrophysics*, *684*, A143. https://doi.org/10.1051/0004-6361/202347489

Donato, G., & Belongie, S. (2002). Approximate thin plate spline mappings. In *Eccv* (Vol. 2, pp. 531–542). Springer Verlag.

Drake, D. J., Schroeder, J. W. R., Howes, G. G., Kletzing, C. A., Skiff, F., Carter, T. A., & Auerbach, D. W. (2013). Alfvén wave collisions, the fundamental building block of plasma turbulence. IV. Laboratory experiment. *Physics of Plasmas*, *20*(7), 072901. https://doi.org/10.1063/1.4813242

Fitzmaurice, A., Drake, J. F., & Swisdak, M. (2025). Ion beam instabilities during solar flare energy release. *Physics of Plasmas*, *32*(4), 042114. https://doi.org/10.1063/5.0260878

Fox, N. J., Velli, M. C., Bale, S. D., Decker, R., Driesman, A., Howard, R. A., et al. (2015). The solar probe plus mission: Humanity's first visit to our star. *Space Science Reviews*, *204*(1–4), 7–48. https://doi.org/10.1007/s11214-015-0211-6

Goodrich, K., Cohen, I. J., Schwartz, S., Wilson, L. B., III, Turner, D., Caspi, A., et al. (2023). The multi-point assessment of the kinematics of shocks (MAKOS). *Frontiers in Astronomy and Space Sciences*, *10*, 1199711. https://doi.org/10.3389/fspas.2023.1199711

Gorman, W., & Klein, K. G. (2024). Mind the gap: Non-local cascades and preferential heating in high-β Alfvénic turbulence. *Monthly Notices of the Royal Astronomical Society*, *531*(1), L1–L7. https://doi.org/10.1093/mnrasl/slae018

He, J., Wang, L., Tu, C., Marsch, E., & Zong, Q. (2015). Evidence of landau and cyclotron resonance between protons and kinetic waves in solar wind turbulence. *The Astrophysical Journal Letters*, *800*(2), L31. https://doi.org/10.1088/2041-8205/800/2/L31

He, J., Wang, Y., Zhu, X., Duan, D., Verscharen, D., & Zhao, G. (2022). Growth of outward propagating fast-Magnetosonic/whistler waves in the inner heliosphere observed by parker solar probe. *The Astrophysical Journal*, *933*(2), 220. https://doi.org/10.3847/1538-4357/ac6c8e

Howes, G. G. (2010). A prescription for the turbulent heating of astrophysical plasmas. *Monthly Notices of the Royal Astronomical Society*, *409*(1), L104–L108. https://doi.org/10.1111/j.1745-3933.2010.00958.x

Howes, G. G. (2024). The fundamental parameters of astrophysical plasma turbulence and its dissipation: Non-relativistic limit. *Journal of Plasma Physics*, *90*(5), 905900504. https://doi.org/10.1017/S0022377824001090

Howes, G. G., Klein, K. G., & TenBarge, J. M. (2014). Validity of the Taylor hypothesis for linear kinetic waves in the weakly collisional solar wind. *The Astrophysical Journal*, *789*(2), 106. https://doi.org/10.1088/0004-637X/789/2/106

Howes, G. G., & Nielson, K. D. (2013). Alfvén wave collisions, the fundamental building block of plasma turbulence. I. Asymptotic solution. *Physics of Plasmas*, *20*(7), 072302. https://doi.org/10.1063/1.4812805

Isenberg, P. A. (2012). A self-consistent marginally stable state for parallel ion cyclotron waves. *Physics of Plasmas*, *19*(3), 032116. https://doi.org/10.1063/1.3697721

Isenberg, P. A., & Vasquez, B. J. (2015). Kinetic evolution of coronal hole protons by imbalanced ion-cyclotron waves: Implications for measurements by solar probe plus. *The Astrophysical Journal*, *808*(2), 119. https://doi.org/10.1088/0004-637X/808/2/119

Jiang, W., Verscharen, D., Jeong, S.-Y., Li, H., Klein, K. G., Owen, C. J., & Wang, C. (2024). Velocity-space signatures of resonant energy transfer between whistler waves and electrons in the Earth's Magnetosheath. *The Astrophysical Journal*, *960*(1), 30. https://doi.org/10.3847/1538-4357/ad0df8

Jiang, W., Verscharen, D., Li, H., Wang, C., & Klein, K. G. (2022). Whistler waves as a signature of converging magnetic holes in space plasmas. *The Astrophysical Journal*, *935*(2), 169. https://doi.org/10.3847/1538-4357/ac7ce2

Kasper, J. C., Abiad, R., Austin, G., Balat-Pichelin, M., Bale, S. D., Belcher, J. W., et al. (2016). Solar wind electrons alphas and protons (SWEAP) investigation: Design of the solar wind and coronal plasma instrument suite for solar probe plus. *Space Science Reviews*, *204*(1–4), 131–186. https://doi.org/10.1007/s11214-015-0206-3

Kennel, C. F., & Petschek, H. E. (1966). Limit on stably trapped particle fluxes. *Journal of Geophysical Research*, *71*, 1–28. https://doi.org/10.1029/jz071i001p00001

Klein, K. G., Howes, G. G., & Brown, C. R. (2025). PLUME: Plasma in a linear uniform magnetized environment. *Research Notes of the American Astronomical Society*, *9*(4), 102. https://doi.org/10.3847/2515-5172/add1c2

Klein, K. G., Howes, G. G., TenBarge, J. M., & Valentini, F. (2020). Diagnosing collisionless energy transfer using field-particle correlations: Alfvén-ion cyclotron turbulence. *Journal of Plasma Physics*, *86*(4), 905860402. https://doi.org/10.1017/S0022377820000689

Klein, K. G., Spence, H., Alexandrova, O., Argall, M., Arzamasskiy, L., Bookbinder, J., et al. (2023). HelioSwarm: A multipoint, multiscale mission to characterize turbulence. *Space Science Reviews*, *219*(8), 74. https://doi.org/10.1007/s11214-023-01019-0

Klein, K. G., & Verscharen, D. (2025). The dielectric response of plasmas with arbitrary gyrotropic velocity distributions. *Physics of Plasmas*, *32*(9), 092104. https://doi.org/10.1063/5.0286477

Klein, K. G., Verscharen, D., Koskela, T., & Stansby, D. (2023). danielver02/alps: Zenodo release [Software]. *Zenodo*. https://doi.org/10.5281/zenodo.8075682

Liu, W., Zhao, J., Wang, T., Dong, X., Kasper, J. C., Bale, S. D., et al. (2023). The radial distribution of ion-scale waves in the inner heliosphere. *The Astrophysical Journal*, *951*(1), 69. https://doi.org/10.3847/1538-4357/acd53b

Livi, R., Larson, D. E., Kasper, J. C., Abiad, R., Case, A. W., Klein, K. G., et al. (2022). The solar probe ANalyzer-Ions on the parker solar probe. *The Astrophysical Journal*, *938*(2), 138. https://doi.org/10.3847/1538-4357/ac93f5

Livi, R., Larson, D. E., & Rahmati, A. (2020). Psp solar wind electrons alphas and protons (sweap) span-a proton differential energy flux for each deflector step, energy, and anode, level 2 (l2), 7 s data [Dataset]. *NASA Space Physics Data Facility*. https://doi.org/10.48322/FTNV-7755

Marsch, E. (2006). Kinetic physics of the solar Corona and solar wind. *Living Reviews in Solar Physics*, *3*, 1. https://doi.org/10.12942/lrsp-2006-1

McManus, M. D., Klein, K. G., Bale, S. D., Bowen, T. A., Huang, J., Larson, D., et al. (2024). Proton- and alpha-driven instabilities in an ion cyclotron wave event. *The Astrophysical Journal*, *961*(1), 142. https://doi.org/10.3847/1538-4357/ad05ba

Meyrand, R., Squire, J., Schekochihin, A. A., & Dorland, W. (2021). On the violation of the zeroth law of turbulence in space plasmas. *Journal of Plasma Physics*, *87*(3), 535870301. https://doi.org/10.1017/S0022377821000489

Moncuquet, M., Meyer-Vernet, N., Issautier, K., Pulupa, M., Bonnell, J. W., Bale, S. D., et al. (2020). First in situ measurements of electron density and temperature from quasi-thermal noise spectroscopy with parker solar Probe/FIELDS. *The Astrophysical Journal Supplement Series*, *246*(2), 44. https://doi.org/10.3847/1538-4365/ab5a84

Nicolaou, G., Wicks, R. T., Rae, I. J., & Kataria, D. O. (2020). Evaluating the performance of a plasma analyzer for a space weather monitor mission concept. *Space Weather*, *18*(12), e2020SW002559. https://doi.org/10.1029/2020SW002559

Powell, M. J. D. (1994). Some algorithms for thin-plate spline interpolation to functions of two variables. In H. P. Dikshit & C. A. Micchelli (Eds.), *Advances in computational mathematics, new Delhi, India* (pp. 303–319). World Scientific.

Quataert, E. (1998). Particle heating by Alfvenic turbulence in hot accretion flows. *The Astrophysical Journal*, *500*(2), 978–991. https://doi.org/10.1086/305770

Raouafi, N. E., Matteini, L., Squire, J., Badman, S. T., Velli, M., Klein, K. G., et al. (2023). Parker solar probe: Four years of discoveries at solar cycle minimum. *Space Science Reviews*, *219*(1), 8. https://doi.org/10.1007/s11214-023-00952-4

Roennmark, K. (1982). Waves in homogeneous, anisotropic multicomponent plasmas (WHAMP). (Tech. Rep.).

Schekochihin, A. A., Cowley, S. C., Dorland, W., Hammett, G. W., Howes, G. G., Quataert, E., & Tatsuno, T. (2009). Astrophysical gyrokinetics: Kinetic and fluid turbulent cascades in magnetized weakly collisional plasmas. *The Astrophysical Journal Supplement Series*, *182*(1), 310–377. https://doi.org/10.1088/0067-0049/182/1/310

Shankarappa, N., Klein, K. G., & Martinović, M. M. (2023). Estimation of turbulent proton and electron heating rates via landau damping constrained by parker solar probe observations. *The Astrophysical Journal*, *946*(2), 85. https://doi.org/10.3847/1538-4357/acb542

Shankarappa, N., Klein, K. G., Martinović, M. M., & Bowen, T. A. (2024). Estimated heating rates due to cyclotron damping of ion-scale waves observed by the parker solar probe. *The Astrophysical Journal*, *973*(1), 20. https://doi.org/10.3847/1538-4357/ad5f2a

Shi, C., Zhao, J., Wu, Y., Liu, S., Xiao, F., & Xie, H. (2025). Generation of sunward ion cyclotron waves and the nature of right-handed polarized ion-scale waves in the near-sun solar wind. *The Astrophysical Journal*, *989*(2), 164. https://doi.org/10.3847/1538-4357/adf43d

Squire, J., Meyrand, R., Kunz, M. W., Arzamasskiy, L., Schekochihin, A. A., & Quataert, E. (2022). High-frequency heating of the solar wind triggered by low-frequency turbulence. *Nature Astronomy*, *6*(6), 715–723. https://doi.org/10.1038/s41550-022-01624-z

TenBarge, J. M., & Howes, G. G. (2013). Current sheets and collisionless damping in kinetic plasma turbulence. *The Astrophysical Journal Letters*, *771*(2), L27. https://doi.org/10.1088/2041-8205/771/2/L27

Verniero, J. L., Chandran, B. D. G., Larson, D. E., Paulson, K., Alterman, B. L., Badman, S., et al. (2022). Strong perpendicular velocity-space diffusion in proton beams observed by Parker solar probe. *The Astrophysical Journal*, *924*(2), 112. https://doi.org/10.3847/1538-4357/ac36d5

Verniero, J. L., Larson, D. E., Livi, R., Rahmati, A., McManus, M. D., Pyakurel, P. S., et al. (2020). Parker solar probe observations of proton beams simultaneous with ion-scale waves. *The Astrophysical Journal Supplement Series*, *248*(1), 5. https://doi.org/10.3847/1538-4365/ab86af

Verscharen, D., & Chandran, B. D. G. (2013). The dispersion relations and instability thresholds of oblique plasma modes in the presence of an ion beam. *The Astrophysical Journal*, *764*(1), 88. https://doi.org/10.1088/0004-637X/764/1/88

Verscharen, D., & Chandran, B. D. G. (2018). NHDS: The New Hampshire dispersion relation solver. *Research Notes of the American Astronomical Society*, *2*(2), 13. https://doi.org/10.3847/2515-5172/aabfe3

Verscharen, D., Klein, K. G., Chandran, B. D. G., Stevens, M. L., Salem, C. S., & Bale, S. D. (2018). ALPS: The arbitrary linear plasma solver. *Journal of Plasma Physics*, *84*(4), 905840403. https://doi.org/10.1017/S0022377818000739

Verscharen, D., Klein, K. G., & Maruca, B. A. (2019). The multi-scale nature of the solar wind. *Living Reviews in Solar Physics*, *16*(1), 5. https://doi.org/10.1007/s41116-019-0021-0

Walters, J., Klein, K. G., Lichko, E., Stevens, M. L., Verscharen, D., & Chandran, B. D. G. (2023). The effects of nonequilibrium velocity distributions on Alfvén ion-Cyclotron waves in the solar wind. *The Astrophysical Journal*, *955*(2), 97. https://doi.org/10.3847/1538-4357/acf1fa

Wilson, L. B., III, Goodrich, K. A., Turner, D. L., Cohen, I. J., Whittlesey, P. L., & Schwartz, S. J. (2022). The need for accurate measurements of thermal velocity distribution functions in the solar wind. *Frontiers in Astronomy and Space Sciences*, *9*, 369. https://doi.org/10.3389/fspas.2022.1063841

Wood, S. N. (2003). Thin plate regression splines. *Journal of the Royal Statistical Society: Series B*, *65*(1), 95–114. https://doi.org/10.1111/1467-9868.00374

Wu, Z., He, J., Duan, D., Zhu, X., Hou, C., Verscharen, D., et al. (2023). Ion energization and thermalization in magnetic reconnection exhaust region in the solar wind. *The Astrophysical Journal*, *951*(2), 98. https://doi.org/10.3847/1538-4357/accf9b

Xie, H.-s. (2019). BO: A unified tool for plasma waves and instabilities analysis. *Computer Physics Communications*, *244*, 343–371. https://doi.org/10.1016/j.cpc.2019.06.014

Zhang, M. F., Kunz, M. W., Squire, J., & Klein, K. G. (2025). Extreme heating of minor ions in imbalanced solar-wind turbulence. *The Astrophysical Journal*, *979*(2), 121. https://doi.org/10.3847/1538-4357/ad95fc

Zhu, X., He, J., Duan, D., Verscharen, D., Owen, C. J., Fedorov, A., et al. (2023). Non-field-aligned proton beams and their roles in the growth of fast Magnetosonic/Whistler waves: Solar Orbiter observations. *The Astrophysical Journal*, *953*(2), 161. https://doi.org/10.3847/1538-4357/acdc17

References From the Supporting Information

Hutchinson, M. F. (1989). A stochastic estimator of the trace of the influence matrix for Laplacian smoothing splines. *Communications in Statistics—Simulation and Computation*, *18*(3), 1059–1076. https://doi.org/10.1080/03610919008812866

Lion, S., Alexandrova, O., & Zaslavsky, A. (2016). Coherent events and spectral shape at ion kinetic scales in the fast solar wind turbulence. *The Astrophysical Journal*, *824*(1), 47. https://doi.org/10.3847/0004-637X/824/1/47

Taylor, G. I. (1938). The spectrum of turbulence. (Vol. 164, pp. 476–490). *Proceedings of the Royal Society of London. Series A—Mathematical and Physical Sciences*. https://doi.org/10.1098/rspa.1938.0032

Torrence, C., & Compo, G. P. (1998). A practical guide to wavelet analysis. *Bulletin of the American Meteorological Society*, *79*(1), 61–78. https://doi.org/10.1175/1520-0477(1998)079⟨0061:APGTWA⟩2.0.CO;2